From inertial to viscous slumping: Numerical and experimental insights of a transient intermediate regime

Alexis Bougouin ◯[*]
Aix-Marseille Université, CNRS, IUSTI, Marseille, France

Laurent Lacaze ◯[†]
*Institut de Mécanique des Fluides de Toulouse (IMFT), Université de Toulouse,
CNRS, INPT, UPS, 31400 Toulouse, France*

The propagation of horizontal dam-break flows induced by the release of a rectangular column of a liquid phase into a negligible ambient fluid is investigated by combining numerical simulations and laboratory experiments. Varying both the geometry of the initial column and liquid properties, the parameter space covered allows the investigation of the transition from inertial to viscous slumping barely considered so far. In light of the Reynolds number Re based on the initial parameters of the fluid column, we report a newly investigated transient regime following the inertial slumping regime and prior to the viscous-dominated one. The transient intermediate regime is shown (i) to only exist for Re $\gtrsim$ 10 and (ii) to be characterized by an inertial overshoot followed by a strong deceleration of the front position accompanied by an excess and a deficit of fluid at the front and at the origin, respectively, with respect to the expected theoretical prediction of the viscous-dominated regime. Beyond the intuitive idea of an adaptive transition from the inertial to fully viscous slumping, these results highlight and quantify the influence of initial inertia on the spreading of a liquid, which may be particularly useful for modeling industrial and geophysical applications.

I. INTRODUCTION

The slumping of a finite-volume liquid column into an ambient fluid along a solid surface has been widely studied at the laboratory scale. One main reason is that this idealized configuration provides most of the dynamical ingredients of unsteady gravity-driven flows encountered in a lot of geophysical and industrial applications. At the geophysical scale, natural hazards, such as avalanches, debris flows and thermal currents, share dynamical processes with this slumping configuration [1]. Dam break or silo collapse are also relevant examples that may initiate unsteady gravity-driven flows of various materials from water to granular medium. At smaller scale, the slump test is a standard tool used to access fluid properties, such as concrete in the mining or food industries [2,3]. Covered by such a variety of applications on various scales, slumping flows became canonical configurations used to extract fundamental dynamical processes through laboratory-scale experiments, numerical simulations, and theoretical models involving Newtonian fluids or more complex materials (Refs. [4–16] among many others).

---

[*]alexis.bougouin@univ-amu.fr
[†]laurent.lacaze@imft.fr

The dynamics of these gravity-driven flows can be split in different flow regimes characterized by the relevant balance of dynamical terms in each regime. For a Newtonian liquid slumping into a weightless and inviscid ambient fluid, well known as the dam-break problem corresponding to one of most popular non-Boussinesq systems, the dynamics is usually split into two main regimes: an inertia-dominated slumping regime characterized by a constant front velocity and a viscous-dominated regime for which the velocity of the front decreases with time and thus the distance of spreading. The inertia-dominated regime has been first investigated by Ritter [4] in the case of a semi-infinite volume of frictionless fluid, for which a theoretical prediction of the height and velocity profiles was proposed based on the shallow-water approximation. In this case, the flow regime is assumed as a balance between inertia and pressure gradient induced by the weight of the slumping liquid. In particular, the theoretical model provides the front velocity $u_f = 2\sqrt{gH}$ and the receding velocity $u_p = -\sqrt{gH}$ of the static/flow frontier, where g is the gravitational acceleration and H is the initial height of the fluid column. In the case of a finite-volume of fluid, this analytical prediction is theoretically applicable as long as the receding perturbation has not reached the back wall, i.e., $t \lesssim L/\sqrt{gH}$ with L the length of the initial column. Thus, the temporal evolution of the front position $x_f^{\text{th}|I}$ and the height profile $h^{\text{th}|I}$ can be summarized as

$$x_f^{\text{th}|I}(t) - L = 2\sqrt{gH}t, \tag{1}$$

$$h^{\text{th}|I}(x,\ t) = \frac{1}{9g}\left(\frac{x_f^{\text{th}|I} - x}{t}\right)^2. \tag{2}$$

Some experimental and numerical studies addressed this regime in the case of water flows propagating in the ambient air. Qualitative agreements are usually obtained with the theoretical front velocity, i.e., the linearity between u_f and $\sqrt{gH}$. However, the quantitative agreement remains questionable as the constant prefactor of u_f is usually found to be smaller than 2 [17–22]. The reason of this discrepancy is usually attributed to bottom dissipation which becomes significant at the front [23–26]. On a longer timescale, the flow may even be totally governed by a balance between the pressure gradient and the inertial drag induced by the bottom wall, which leads to a front propagation as $x_f \propto t^{2/5}$ [25]. Thus, such observations suggest some intermediate regimes between the purely inertial regime unaffected by any dissipation, and a purely viscous one.

In the viscous-dominated regime, viscous dissipation overcomes inertia over the entire slumping phase and consequently slows the current down. A self-similar solution has been derived from lubrication theory, balancing viscous stress and pressure gradient. In this case, both the front position and the height profile are found as

$$x_f^{\text{th}|V}(t) = \eta_n\left[\frac{\rho g(HL)^3 t}{3\mu}\right]^{1/5}, \tag{3}$$

$$h^{\text{th}|V}(x,\ t) = (3/10)^{1/3}\eta_n^{2/3}\left[\frac{3\mu(HL)^2}{\rho g t}\right]^{1/5} f^{\text{th}}(x,\ t) \equiv (3/10)^{1/3}\eta_n^{5/3}\frac{HL}{x_f^{\text{th}|V}} f^{\text{th}}\left(x/x_f^{\text{th}|V}\right), \tag{4}$$

where $\eta_n \sim 1.411$ is a constant, ρ and μ are the density and the viscosity of the slumping fluid, respectively, H and L are the height and length of the initial column, respectively, and $f^{\text{th}}(x/x_f^{\text{th}|V}) = [1 - (x/x_f^{\text{th}|V})^2]^{1/3}$ is an analytical function [5]. Note that such a solution is not expected to hold close to the initial state, being therefore valid on a relatively long timescale [27,28]. This theoretical solution can be used as long as capillary effects can be disregarded, i.e., the height of the current is larger than the capillary length.

In the context of gravity currents, i.e., when the density difference between the surrounding fluid and the slumping phase is small enough, some experimental studies focused especially on the inertial-to-viscous transition (e.g., Refs. [7,29]). In this case, an intermediate inertial regime is usually reported, referred to as the inertial-buoyancy regime, prior the viscous-dominated regime
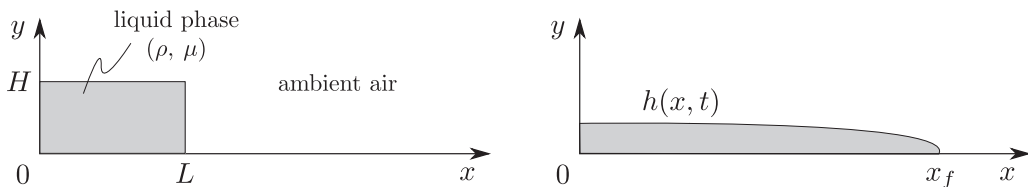
FIG. 1. Sketch of the initial geometry (left) and the slumping flow (right) for the 2D dam-break configuration.

mentioned above [7]. It is attributed to the finite size of the initial reservoir affecting the current front, thus evolving as $x_f \propto t^{2/3}$. However, this inertial-buoyancy regime is not expected for dam-break flows because the front travels as fast as the propagating perturbation [30]. It therefore leaves bottom drag invading the entire flow prior fully developed viscous flow as the only mechanism of intermediate regime.

First disregarding such intermediate regime, the entire dynamics of a dam-break flow starting from an inertial-dominated regime toward a fully viscous regime, would be therefore modeled by matching the two previous theoretical models. The intermediate regime could therefore be seen as a continuous and monotonic transition linking these scalings on a finite time interval and a finite length. In the present contribution, we show, however, that the inertia-to-viscous transient dynamics of horizontal dam-break flows is more complex than expected from numerical simulations and laboratory experiments. Following this objective, this study aims at characterizing the inertia-to-viscous transition in the specific configuration of a Newtonian liquid released into the ambient air. The paper is organized as follows. In Sec. II, both numerical simulations and laboratory experiments are presented and compared together. Then first observations of the transient dynamics following the inertial slumping regime and prior to the viscous-dominated one are addressed based on a dimensional analysis (Sec. III). Section IV is dedicated to the fine characterization of the transient intermediate regime providing scaling laws of different extracted quantities. Finally, we dicuss the limitations of the results presented along the paper offering future perspectives (Sec. V).

II. SLUMPING SETUP

A. Methodology

In the present study, a two-dimensional (2D) dam-break configuration is used as shown in Fig. 1. Both the initial geometry and the slumping flow are described in the (x, y) plane, with x and y the horizontal and vertical directions, respectively, while the spanwise z direction is disregarded. The setup consists of a rectangular reservoir of length L filled with a dense fluid of density ρ and dynamic viscosity μ up to a height H. At $t = 0$, the initial column is released in air, and the dense fluid slumps along the horizontal plane. Such an idealized configuration is particularly useful to capture main physical processes of hydrostatic shallow-layer flows encountered in plenty of industrial and geophysical applications.

The 2D numerical simulations are performed with the open-source computational fluid dynamics code OpenFOAM [31]. The InterFoam solver is used which allows to describe the flow dynamics of two Newtonian, incompressible and immiscible fluids using the volume-of-fluid method, one being the slumping phase (ρ, μ) and the other ambient air $(\rho_a, \mu_a) = (1.2 \text{ kg m}^{-3}, 1.8 \times 10^{-5} \text{ Pa s})$. No surface tension are considered between the two phases, as it plays no role on the scales considered here. No-slip boundary conditions are imposed at the back and bottom walls of the domain and the domain size is dependent on the length scales of the problem, i.e., the distance necessary to reach the viscous regime in the x direction and the initial height of the column in the y direction. For all simulations, the spatial resolution of the mesh is set to $\Delta x = 2$ mm and $\Delta y = 0.5$ mm in the streamwise and vertical directions, respectively. No significant differences were obtained on

the results presented here when decreasing the mesh size or changing the cell aspect ratio. For numerical simulations, the height and the length of the initial column are varied in the range $H = [0.01 : 0.2]$ m and $L = [0.05 : 0.5]$ m, respectively.

The laboratory experiments are conducted in a horizontal transparent channel of rectangular cross section. The dimensions of the channel are 1.6 m long, 0.5 m high, and 0.2 m wide along the streamwise x, vertical y, and spanwise z coordinates, respectively. The finite-volume reservoir is delimited by a sluice gate at $x = L = 0.1$ m from one side of the channel. Three different heights of liquid characterizing the initial column geometry are used, namely $H = 0.05, \ 0.1$, and 0.2 m. The initial time $t = 0$ is chosen as the initial motion of the gate manually lifted up in approximately 0.1 s. The release time of the gate is of the order of the inertial timescale $(H/g)^{1/2}$, suggesting the slumping dynamics could be affected as discussed later. The slumping flow is then recorded in the $(x, \ y)$ plane with a Lavision 2560×2160 pixels camera using a shadowgraphy method. The obtained resolution is about 500 μm/pixel, and the acquisition frequency is between 10 and 108 Hz depending on the timescale of the flow. For all experiments, the liquid phase used is a mixture of water and Ucon oil 75H90000 (a Newtonian fluid soluble in water). The relative concentration of Ucon oil and water, defined as $c_m = m_o/(m_o + m_w)$, with m_o and m_w the mass of oil and water, respectively, allows us to vary the viscosity and consequently the density of the fluid (more details given in Ref. [32]). In this study, four different mixtures are considered with a mass fraction c_m of 11%, 28%, 49%, and 73%, leading to a viscosity and a density of $\mu = [0.01, \ 0.1, \ 1, \ 10]$ Pa s and $\rho = [1015, \ 1040, \ 1075, \ 1093]$ kg m^{-3}, respectively. The viscosity of the fluid is measured using a cone-plate geometry in a Haake Mars III rheometer, and the density is estimated with a calibration curve.

In the case of a dam-break configuration, as the ambient air is supposed to be inactive, the slumping dynamics is mainly controlled by a balance between the pressure gradient and inertia or viscous dissipation depending on the flow regime considered (see Sec. I). Thus, it follows that the propagation of the slumping can be described in terms of a unique dimensionless parameter, namely the Reynolds number $\mathrm{Re} = \rho(gH)^{1/2}H^2/\mu L$, comparing the relative influence of inertia, based on a horizontal hydrostatic pressure gradient, and viscous dissipation at the flow scale. In the present study, it is varied in the range $\mathrm{Re} = [0.2 : 6 \times 10^4]$. The wide range of Re considered allows to anticipate both inertia- and viscous-dominated regimes with a transition from one to the other during the propagation of the slumping, at sufficiently large Re. Although the following results confirms the relevance of Re for describing the slumping flow, it can be split into two different contributions as $\mathrm{Re} = a\mathrm{Re}^H$. Here the Reynolds number $\mathrm{Re}^H = \rho(gH)^{1/2}H/\mu$ is based on vertical fall of the initial column, which then introduces the initial aspect ratio $a = H/L$ of the fluid column. Note that Re^H is probably more relevant to characterize viscous dissipation during initial stages of the flow, while the former Re characterizes viscous dissipation during the horizontal spreading of the liquid on a longer timescale. Thus, both are varied in the range $\mathrm{Re}^H = [3.4 : 3 \times 10^4]$ and $a = [0.05 : 2.5]$, respectively. Finally, for laboratory experiments, the surface tension could prevail close to the front, which may be quantified through a Bond number Bo based on the slumping properties. Here one obtains $\mathrm{Bo} = \rho g h^2/\sigma \gtrsim 5$, where $\sigma = 0.055$ N m^{-1} is the surface tension of water/Ucon oil mixtures [32], $h = HL/l$ is the characteristic height of the slumping and $l \sim 1$ m is the typical length of the channel. Such values of Bo prevents from any influence of the surface tension on the front dynamics of the slumping phase.

B. Numerical and experimental comparison

Numerical simulations and laboratory experiments have been first performed considering the same initial conditions and thus the same Reynolds number Re. Figure 2 shows the temporal evolution of the slumping height profile $h(x, t)$ extracted from (a) the numerical simulations and (b) the experiments, with $\mathrm{Re} = 10^3$. The global trend of the slumping flow is broadly similar despite some quantitative discrepancies, which can be attributed to both numerical approximations and experimental uncertainties. In particular, the numerical front evolves faster than its experimental
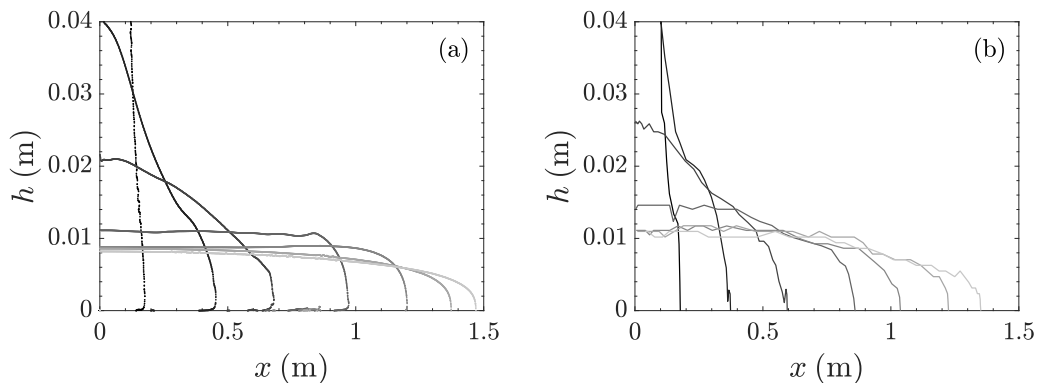
FIG. 2. Temporal evolution of the slumping height profile $h(x, t)$ extracted from (a) the numerical simulations and (b) the laboratory experiments, with Re $= 10^3$. The height profiles are shown at $t = 0.1, 0.3, 0.5, 1, 2, 8,$ and 16 s (from dark to light gray). Here the horizontal and vertical dimensions of the initial column are $L = H = 0.1$ m, respectively.

counterpart, which may be attributed to 2D simulations that underestimate total dissipation induced by back and bottom walls in the experiments, or the release system which differs between the two approaches. As previously discussed in Sec. II A, the release timescale is equivalent to the inertial flow timescale $(H/g)^{1/2}$ in experiments, while it is instantaneous in numerical simulations. At early times, the falling motion of the slumping phase is thus initiated in presence of the sluice gate for experiments, which may promote additional dissipation in the system compared to numerical simulations. On the other hand, it shall be noted that the relevant boundary condition of numerical model to be considered at the bottom wall is not obvious [33]. Imposing no-slip boundary condition for both the slumping phase and the ambient fluid induces an initial motionless front, which leads to the formation of a thin layer of ambient fluid below the slumping phase reducing viscous dissipation. Different numerical tricks were proposed to limit this phenomenon [33], but such modification of boundary conditions still suffer a better knowledge of the local interaction between the slumping phase and the bottom wall (e.g., wettability) in laboratory experiments. As the global dynamics related to processes discussed later are captured by numerical simulations, we prefer to keep boundary conditions as no-slip without a better knowledge of local processes at the triple point in experiments.

In order to strengthen the reliability of simulations to capture the main processes of the slumping flow, Fig. 3 compares the temporal evolution of the front position $x_f(t)$ obtained with numerical simulations (solid lines) and experiments (crosses) for different Re. At early stages, the front position follows a linear evolution with time, i.e., $x_f \propto t$, corresponding to the inertial slumping regime as defined by Eq. (1). Later, the front velocity of currents smoothly decreases, thus leaving the inertial regime, and viscous dissipation cannot be disregarded any longer. The slumping eventually reaches a purely viscous-dominated regime, during which the front position follows Eq. (3). The comparison with both inertial and viscous theoretical predictions will be more fully addressed in Sec. III. As discussed previously, some quantitative discrepancies below 10% for the local front position $x_f(t)$ may be reported, but the global evolution from inertial- to viscous-dominated regimes is consistent between the experiments and the numerical simulations. Moreover, these discrepancies are relatively low compared to those associated with the variations of the Reynolds number Re. Thus, it can be concluded that both approaches describe properly the slumping dynamics, while numerical simulations provide a relevant and useful tool to highlight the main physical processes of the slumping by modifying easily the geometry of the initial column and fluid properties and thus the Reynolds number Re. In the following, the numerical simulations will be thus mostly used to characterize the transient dynamics from the inertial slumping regime to the fully viscous one.
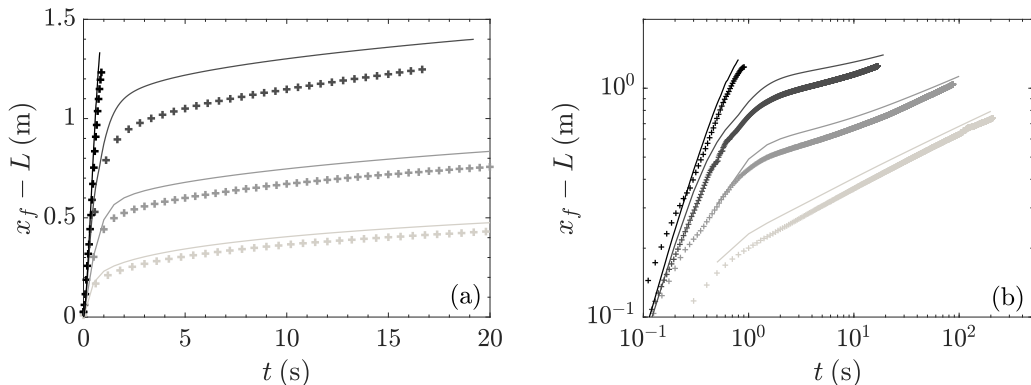
FIG. 3. (a) Lin-lin and (b) log-log representation of the temporal evolution of the front position $x_f - L$ obtained with numerical simulations (solid lines) and laboratory experiments (crosses), for Re = [19, 182, 1030, 5827] [from light to dark gray]. The horizontal and vertical dimensions of the initial column are $L = 0.1$ m and $H = [0.05, 0.05, 0.1, 0.2]$ m, respectively.

III. FROM INERTIAL TO VISCOUS FLOW REGIMES

A. Dimensionless scalings

The Reynolds number Re as defined previously, is based on the horizontal and vertical length scales L and H, respectively, and the associated timescale is $L/\sqrt{gH}$ for describing the spatiotemporal evolution of the slumping. Accordingly, the dimensionless front position $\tilde{x}_f = x_f/L$, the dimensionless height profile $\tilde{h} = h/H$, and the dimensionless time $\tilde{t} = t\sqrt{gH}/L$ are defined, and the theoretical solutions given by Eqs. (1) and (3) are therefore rewritten as

$$\tilde{x}_f^{\text{th}|I} - 1 = 2\tilde{t}, \tag{5}$$

$$\tilde{x}_f^{\text{th}|V} = \eta_n \left(\frac{\text{Re}}{3}\tilde{t}\right)^{1/5}. \tag{6}$$

We can then define a transition time $\tilde{T}_v$ between the two regimes by equalizing the two spreading laws of $\tilde{x}_f$ [Eqs. (5) and (6)] obtained in both inertial and viscous regimes. As already stated, the viscous theoretical solution [Eq. (6)] is only valid relatively far from the initial condition under the shallow-layer approximation, which may be written as $\tilde{x}_f^{\text{th}|V} > 1$ and $\tilde{x}_f^{\text{th}|V} > a^{1/2}$, respectively. Thus, one solves this balance problem in asymptotic limit, leading to the explicit estimate

$$\tilde{T}_v = \left(\frac{\eta_n}{2}\right)^{5/4}\left(\frac{\text{Re}}{3}\right)^{1/4} \quad \text{and} \quad \tilde{x}_f^{\text{th}}(\tilde{T}_v) = \eta_n^{5/4}\left(\frac{\text{Re}}{6}\right)^{1/4}, \tag{7}$$

valid if Re > 1 and Re > a^2 [as $\tilde{x}_f^{\text{th}}(\tilde{T}_v) > 1$ and $\tilde{x}_f^{\text{th}}(\tilde{T}_v) > a^{1/2}$]. In the present study, we mostly satisfy this condition, for which the above scalings and the unique Re dependency are thus expected to be relevant. Note that, for Re < 1, the slumping should enter instantaneously a viscous regime, or more precisely on a typical length of spreading smaller than the initial length of the column, when the dense fluid is released. Thus, the condition Re ~ 1 corresponds to the transition between a purely viscous regime (i.e., when Re < 1) and a combined inertia-to-viscous regime (i.e., when Re > 1) of the slumping. To finish, Eq. (7) highlights another limiting behavior. In the parameter space (Re, a), approaching Re $\sim a^2$ from below indicates that the shallow-layer condition is less applicable. Above Re $\sim a^2$, the transition from the inertial slumping toward the viscous slumping dynamics is thus expected to occur during the vertical falling acceleration of the slumping, for which
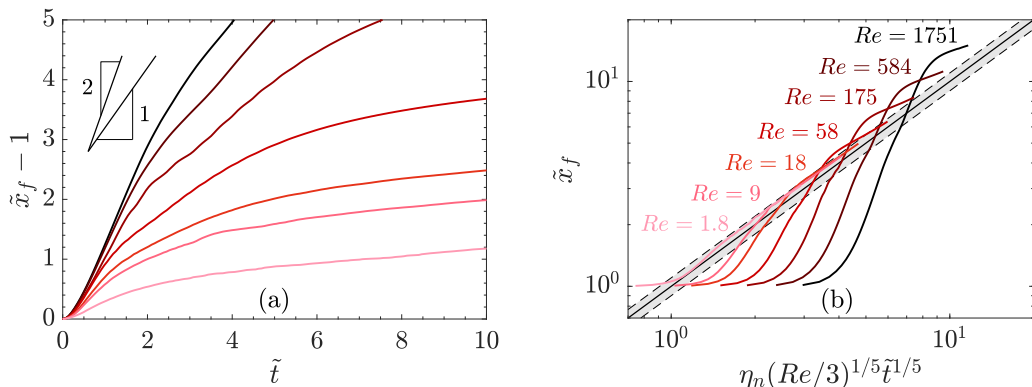
FIG. 4. Temporal evolution of the dimensionless front position $\tilde{x}_f$ obtained from numerical simulations. Axis scales are chosen according to (a) inertial [Eq. (5)] and (b) viscous [Eq. (6)] solutions. In (b), the solid and dashed lines correspond to the viscous solution [Eq. (6)] with a deviation of $\pm 10\%$.

the couple (Re^H, a) is probably the most relevant parameters for describing it (more details given in Sec. V).

B. Dimensionless flow dynamics: Observations from numerical simulations

Now the evolution of the front position and the height profile of the slumping can be addressed according to the inertial and viscous dimensionless solutions. Based on the scaling analysis presented above, the slumping dynamics is investigated by varying incrementally the Reynolds number Re.

Figure 4 shows the dimensionless front position $\tilde{x}_f$ as a function of the expected timescale according to the inertial [Eq. (5)] and viscous [Eq. (6)] solutions. At early times, i.e., for $\tilde{t} \lesssim 0.5$, the spreading front first accelerates corresponding to the transition from the initial static column toward the flow dynamics of the slumping liquid [Fig. 4(a)]. This initial acceleration can be described as a free-fall motion of the slumping front, at least at sufficiently large Re [34]. Then the front position evolution clearly follows an inertial regime characterized by a constant front velocity. The initial slope of $\tilde{x}_f(\tilde{t})$ depends on Re ranging roughly from 1 to 2, as already reported in the literature (e.g., Refs. [19–22,24]). A smaller slope value than the expected one of two from the inertial formulation [Eq. (5)] with decreasing Re is consistent with local viscous dissipation, which means that part of the transition toward the viscous regime has already started. Then the lowest value of Re = 1.8, close to the condition Re $\sim$ 1, leads to a nearly initially viscous dynamics of the flow. Contrary to the usual view of a smaller coefficient of the inertial trend, one can conclude that the transition toward an expected viscous regime occurs at earlier times with decreasing Re, which is consistent with the estimate of $\tilde{T}_v$ given by Eq. (7). At longer times, the viscous dimensionless scaling according to the theoretical solution [Eq. (6)] then becomes relevant to describe the temporal evolution of the slumping [solid line, in Fig. 4(b)]. Recall that even for a purely viscous slumping, i.e., Re = 1.8 here [Fig. 4(b)], the theoretical solution [Eq. (6)] cannot describe the front position evolution of a purely viscous slumping at early times because of the dependency on the initial state of the slumping liquid. The dashed lines represent the deviation of the front compared to the theoretical prediction of around 10% due to numerical uncertainties, as discussed in Sec. II B. Again one observes that the inertial-to-viscous transition occurs earlier for decreasing Re as predicted by the estimate of $\tilde{T}_v$ [Eq. (7)].

In most of the cases discussed here, the front position evolution shows that the slumping does not evolve monotonically from the inertial slumping regime to the viscous-dominated one. At large Re, it is clearly highlighted that the front position $\tilde{x}_f$ overshoots the expected viscous solution
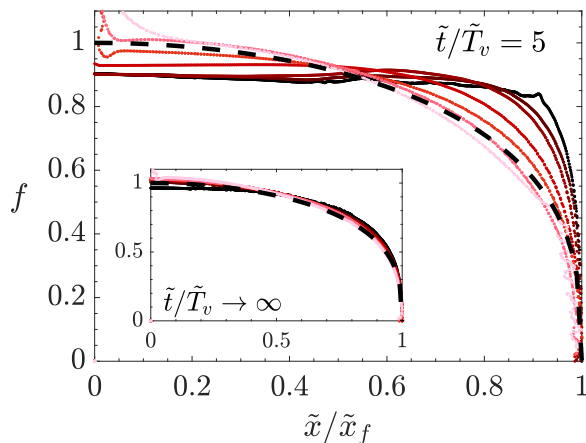
FIG. 5. The shape function f as a function of the normalized streamwise direction $\tilde{x}/\tilde{x}_f$, at $\tilde{t}/\tilde{T}_v = 5$ (inset: at $\tilde{t}/\tilde{T}_v \to \infty$), for the same set of simulations shown in Fig. 4. The black dashed line corresponds to the viscous theoretical shape function $f^{\text{th}}(\tilde{x}/\tilde{x}_f) = [1 - (\tilde{x}/\tilde{x}_f)^2]^{1/3}$.

[Fig. 4(b)]. This implies a strong deceleration of the front to reach the viscous solution from above at longer times. This behavior cannot be fully attributed to the inertial bottom drag counterbalancing the pressure gradient as such a situation would lead to a monotonic evolution of the front position as $x_f \propto t^{2/5}$ [25], unrecovered here. To our knowledge, this transient intermediate regime has never been reported so far probably due to a main interest on purely inertial and viscous dam-break flows, disregarding the transition from one to the other during which both inertia and viscous forces should be considered.

When the slumping enters the viscous regime at $\tilde{t} > \tilde{T}_v$, the dimensionless height profile should follow

$$\tilde{h}^{\text{th}|V}(x, \, t) = (3/10)^{1/3} \eta_n^{5/3} \big(\tilde{x}_f^{\text{th}|V}\big)^{-1} f^{\text{th}}\big(\tilde{x}/\tilde{x}_f^{\text{th}|V}\big), \tag{8}$$

according to the viscous self-similar solution [Eq. (4)] in a dimensionless form. Moreover, the analytical form of the inertial solution [Eq. (2)] implies that the height profile should evolve toward the viscous solution [Eq. (4)] from above and below at the origin and the front, respectively. The shape function of currents is extracted from numerical simulations as $f = \tilde{h}\tilde{x}_f/(3/10)^{1/3} \eta_n^{5/3}$ according to Eq. (8). Figure 5 shows the shape function f as a function of the normalized streamwise direction $\tilde{x}/\tilde{x}_f$, at $\tilde{t}/\tilde{T}_v = 5$ (inset: at $\tilde{t}/\tilde{T}_v \to \infty$, i.e., $\tilde{t} \gg \tilde{T}_v$) for the same set of simulations shown in Fig. 4. For comparison, the viscous theoretical shape function f^{th} is also plotted as the black dashed line. Overall, the height profile is characterized by a monotonous decrease on the whole range of $0 \lesssim \tilde{x}/\tilde{x}_f \lesssim 1$. However, the height at the origin, i.e., $f(\tilde{x}/\tilde{x}_f = 0)$, and the frontal height, i.e., $f(\tilde{x}/\tilde{x}_f \to 1)$, can be significantly smaller and larger than the viscous prediction, respectively. The decrease of Re leads to a better prediction of the shape profile, at $\tilde{t}/\tilde{T}_v = 5$ (light red). This indicate that the existence of an initial inertial regime influences the behavior of the slumping shape by pushing additional fluid from the origin to the front during the transient stage. In particular, when increasing Re (from light to dark red), a deficit and an excess of fluid at the origin and at the front, respectively, is clearly observed in comparison with the viscous prediction. Moreover, the emergence of the blunt front shape occurs simultaneously with the overshoot of the front position previously mentioned. At long times (i.e., $\tilde{t}/\tilde{T}_v \to \infty$), however, the viscous self-similar solution of the height profile is still recovered, regardless of the value of Re (inset of Fig. 5).

These results confirm the relevance of the inertial and viscous self-similar solutions to predict the evolution of the slumping at early and late stages. However, we showed the existence of a transient intermediate regime following the inertial slumping regime and prior to the viscous-dominated one,
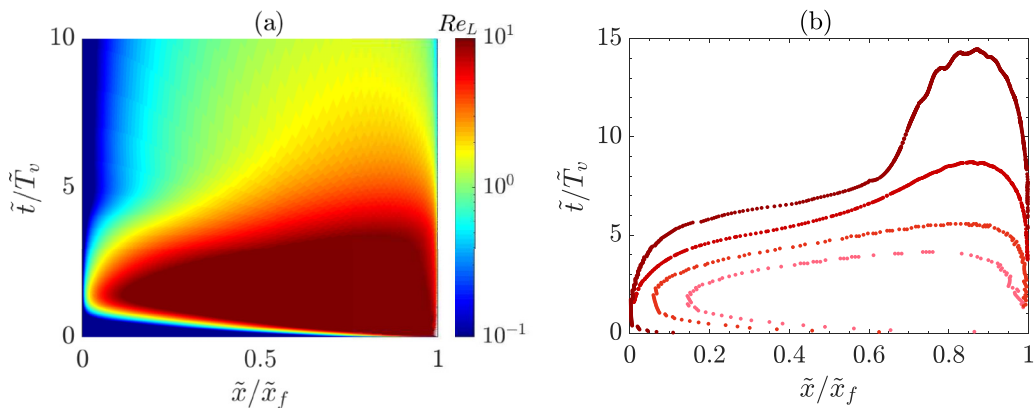
FIG. 6. (a) Spatiotemporal evolution of the local Reynolds number Re_L [Eq. (9)] as a function of $\tilde{x}/\tilde{x}_f$ and $\tilde{t}/\tilde{T}_v$, with $\mathrm{Re} = 12$. (b) The $\{\mathrm{Re}_L = 1\}$ contour as a function of $\tilde{x}/\tilde{x}_f$ and $\tilde{t}/\tilde{T}_v$ for $\mathrm{Re} = [9, 18, 58, 175]$ (from light to dark red).

which is mainly controlled by the Reynolds number Re. It is characterized by an overshoot followed by a strong deceleration of the front position accompanied by a deficit and an excess of fluid at the origin and at the front, respectively, in comparison with the expected viscous theoretical solution.

C. A spatiotemporal inertial-to-viscous transition

In Sec. III A, a scaling analysis was proposed to quantify the time and length scales of a sudden transition from the inertial- to the viscous-dominated regime of the slumping. Not surprisingly, the intermediate regime previously shown indicates a more complex evolution during the propagation. In particular, the spatiotemporal evolution of the dynamics within the slumping body has to be considered. In this way, the streamwise and time-dependent local Reynolds number is defined as follows:

$$\mathrm{Re}_L(x, t) = \frac{\rho \bar{u}(x, t) h(x, t)}{\mu} \quad \text{with} \quad \bar{u}(x, t) = \frac{1}{h(x, t)} \int_0^h u(x, y, t) dy, \tag{9}$$

where $\bar{u}(x, t)$ and $u(x, y, t)$ are the depth-averaged and local streamwise velocities, respectively and $h(x, t)$ is the height profile of the slumping.

Figure 6(a) shows the evolution of Re_L as a function of $\tilde{x}/\tilde{x}_f$ and $\tilde{t}/\tilde{T}_v$, with $\mathrm{Re} = 12$. As anticipated, the slumping highlights a more complex dynamics than the idealized gradual inertial-to-viscous transition that would lead to no color variation along the streamwise direction. Here the spatiotemporal evolution of the slumping can be split in both inertia- and viscous-dominated regions in the ($\tilde{x}/\tilde{x}_f$, $\tilde{t}/\tilde{T}_v$) space. More specifically, we consider the inertial and viscous domains as the regions for which $\mathrm{Re}_L > 1$ and $\mathrm{Re}_L < 1$, respectively, mostly in red and blue colors in Fig. 6(a). The $\{\mathrm{Re}_L = 1\}$ contour thus highlights the spatiotemporal transition from inertial- to viscous-dominated regions whithin the slumping body.

Figure 6(b) shows the $\{\mathrm{Re}_L = 1\}$ contour as a function of $\tilde{x}/\tilde{x}_f$ and $\tilde{t}/\tilde{T}_v$ for Re increasing (from light to dark red). One observes that the viscous-dominated dynamics invades the slumping phase from both the front and the back wall. This viscous invasion leaves a persisting region of inertial dynamics close to the front, thus revealing a spatial coexistence of an inertial and two viscous domains over a finite time interval. The increase of Re promotes more significant inertial regions persisting over a long timescale well above the viscous time $\tilde{T}_v$, and this inertial dynamics is therefore predisposed to disturb the front dynamics of the slumping.
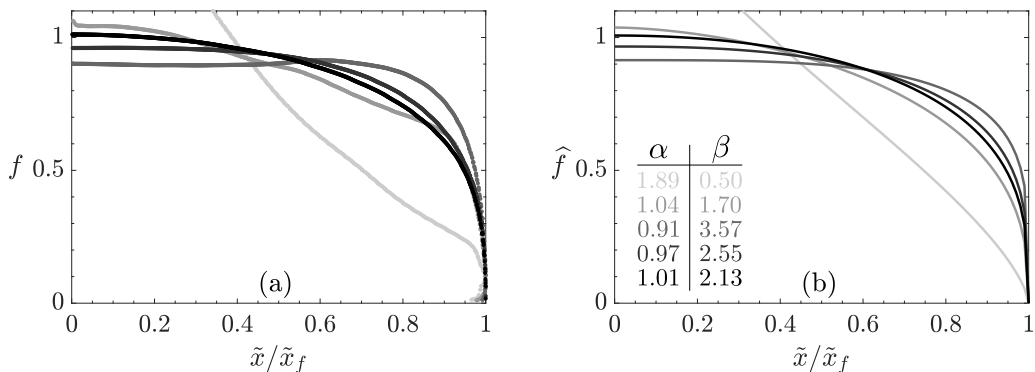
FIG. 7. (a) The shape function $f = \tilde{h}\tilde{x}_f/(3/10)^{1/3}\eta_n^{5/3}$ extracted from the numerical simulations and (b) the fitted shape solution $\widehat{f}$ [Eq. (10)] as a function of the normalized streamwise direction $\tilde{x}/\tilde{x}_f$, at $\tilde{t}/\tilde{T}_v = 1, 2, 5, 10,$ and 20 (from light to dark gray), with Re $\sim$ 175.

IV. CHARACTERIZATION OF THE TRANSIENT INTERMEDIATE REGIME

A. Quantifying the intermediate regime

The nontrivial inertial-to-viscous transition within the slumping body could explain the overshoot of the front position and the excess (respectively, deficit) of fluid at the front (respectively, at the origin), in comparison with the viscous theoretical solution (Figs. 4 and 5). This is interpreted as a newly transient adaptation regime following the inertial slumping regime and prior entering the viscous one. Because of the complexity of the intermediate regime including a balance of inertia and viscous forces within the slumping body (see Sec. III C), no theoretical background exists to predict the temporal evolution of the front position and the height profile. For this reason, we propose to quantify the intermediate regime through the deviation of different extracted quantities from the theoretical viscous prediction [Eqs. (6) and (8)]. To achieve this, we extend empirically the shape function f^{th} found from the viscous theory to describe the shape of the slumping phase during its entire propagation, as

$$\widehat{f} = \alpha\left[1 - \left(\frac{\tilde{x}}{\tilde{x}_f}\right)^{\beta}\right]^{1/(\beta+1)}, \tag{10}$$

where α and β are unknown fitting parameters quantifying the height at the origin, i.e., $\widehat{f}(\tilde{x}/\tilde{x}_f = 0) = \alpha$, and the blunting of the height profile, respectively. Note that the shape function given by Eq. (10) has no specific mathematical background, except for the values of $\alpha^{\mathrm{th}|V} = 1$ and $\beta^{\mathrm{th}|V} = 2$ recovering the viscous asymptotic prediction. Nevertheless, this description allows to explicitly incorporate temporal and spatial dependencies of the slumping on Re for the purpose of quantifying its relative influence onto $\tilde{x}_f$, α, and β.

In order to highlight the relevance of the empirical function $\widehat{f}$ [Eq. (10)] to capture the shape of the slumping, and particularly, during the transient intermediate regime, an example of (a) the shape function f extracted from the numerical simulations and (b) the fitted shape function $\widehat{f}$ with t increasing (from light to dark gray), for Re $\sim$ 175, is shown in Fig. 7. One observes the relevance of this description which actually provides a reasonable evolution of shape profiles, at different times of the slumping dynamics. In particular, the proposed shape function allows to provide the shape of the slumping interface from the inertial regime (light gray), quite surprisingly, toward the viscous one (dark gray), therefore including the transient intermediate regime characterized by a deficit and an excess of fluid at the origin and at the front, respectively, with respect to the viscous theoretical shape function. We thus assert that, despite an empirical basis, the modified shape function $\widehat{f}$ contains the ingredients needed to describe the intermediate regime in the following.
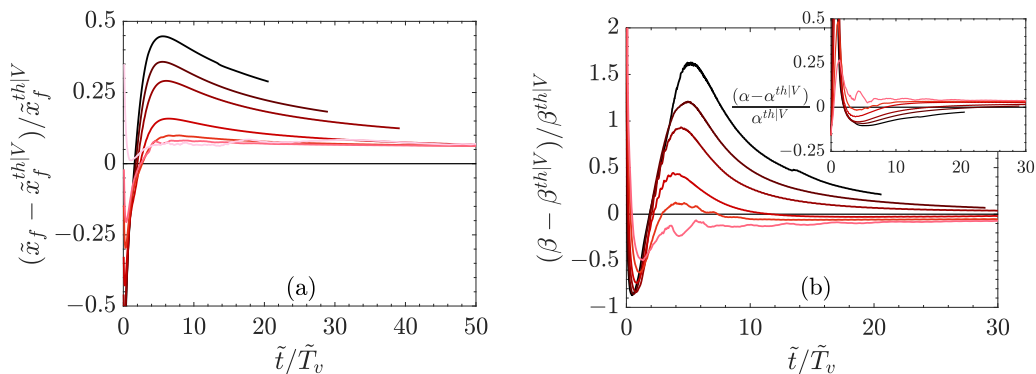
FIG. 8. (a) $(\tilde{x}_f - \tilde{x}_f^{\text{th}|V})/\tilde{x}_f^{\text{th}|V}$ and (b) $(\beta - \beta^{\text{th}|V})/\beta^{\text{th}|V}$ [inset: $(\alpha - \alpha^{\text{th}|V})/\alpha^{\text{th}|V}$] as a function of normalized time $\tilde{t}/\tilde{T}_v$, with Re $\in [1.8 : 1751]$ (from light to dark red). Horizontal solid lines correspond to the viscous theoretical solution with $\tilde{x}_f^{\text{th}|V}$ given by Eq. (6), $\alpha^{\text{th}|V} = 1$ and $\beta^{\text{th}|V} = 2$.

Now the deviation of the transient intermediate regime from the viscous one can be quantified through the discrepancy of the extracted quantities with respect to the viscous theoretical solution as $(\tilde{x}_f - \tilde{x}_f^{\text{th}|V})/\tilde{x}_f^{\text{th}|V}$, $(\alpha - \alpha^{\text{th}|V})/\alpha^{\text{th}|V}$, and $(\beta - \beta^{\text{th}|V})/\beta^{\text{th}|V}$, where $\tilde{x}_f^{\text{th}|V}$ is given by Eq. (6), $\alpha^{\text{th}|V} = 1$, and $\beta^{\text{th}|V} = 2$. Figure 8 shows these different quantities plotted as a function of normalized time $\tilde{t}/\tilde{T}_v$, for Re increasing (from light to dark red). In most of the cases, the quantities cross the viscous theoretical solution (solid lines) around $\tilde{t}/\tilde{T}_V \approx 2$. Then $(\tilde{x}_f - \tilde{x}_f^{\text{th}|V})/\tilde{x}_f^{\text{th}|V}$ and $(\beta - \beta^{\text{th}|V})/\beta^{\text{th}|V}$ overshoot and $(\alpha - \alpha^{\text{th}|V})/\alpha^{\text{th}|V}$ undershoots the viscous theoretical solution before tending asymptotically toward it at longer times. In fact, the asymptotic value of both $(\alpha - \alpha^{\text{th}|V})/\alpha^{\text{th}|V}$ and $(\tilde{x}_f - \tilde{x}_f^{\text{th}|V})/\tilde{x}_f^{\text{th}|V}$ is not exactly zero. At long times, the overestimate of α compared to $\alpha^{\text{th}|V}$ can be probably attributed to the no-slip condition imposed along the back wall affecting the slumping height at the origin. In the same way, the no-slip boundary condition at the bottom wall considered in numerical simulations is expected to reduce total dissipation through the formation of a thin layer of ambient fluid between the slumping phase and the bottom surface, as previously discussed in Sec. II B, which differs from the viscous theoretical solution. In any case, this quantitative bias does not modify the analyses and conclusions drawn here, and it will be taken into account by adding error bars in the following. Finally, the similar trend of all quantities supports the presence of an intermediate regime prior the viscous-dominated one, as well as the relevance of this description to characterize it. As expected, this behavior and the related transient intermediate regime is hardly observed for smaller Re (light red). The transient intermediate regime can therefore be characterized by the deviation of $\tilde{x}_f$, α, and β from the asymptotic viscous solution, which clearly increases with increasing Re.

It can also be concluded from Fig. 8 that $\tilde{T}_v$ is more relevant to provide the transition time from the inertial regime to the intermediate one, instead of predicting the transition time toward the viscous-dominated regime as initially derived. We obtain here $\tilde{t}/\tilde{T}_V \approx 2$ as the relevant timescale of the beginning of the intermediate regime. By analogy with the intermediate inertial regime of gravity currents following the inertial slumping and prior to the viscous one (see Sec. I), the beginning of the transient intermediate regime can be interpreted as the time at which the back wall reflected perturbation reaches the slumping front, which is only possible when the front is slowed down by viscous dissipation and thus enters the viscous-dominated regime. The timescale of the receding perturbation can be expressed as $\tilde{T}_p = 1 + \tilde{x}_f^{\text{th}}(\tilde{T}_v) \approx \eta_n^{5/4}(\text{Re}/6)^{1/4}$, knowing that $\tilde{x}_f^{\text{th}} > 1$ (Sec. III A). This leads to $\tilde{T}_p/\tilde{T}_v = 2$ consistent with the time at which the transient regime occurs and this inertial perturbation is thus probably at the origin of the transient intermediate regime. For
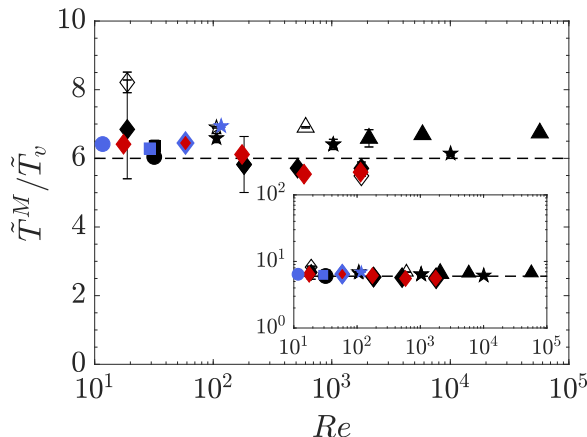
FIG. 9. Timescale ratio $\tilde{T}^M/\tilde{T}_v$ as a function of the Reynolds number Re, for numerical (closed symbols) and experimental (opened symbols) results. The red and blue colors correspond to the set of simulations at constant $a = 0.5$ and constant $\mathrm{Re}^H \sim 117$, respectively, while the symbols indicate the initial aspect ratio as (•) $a = 0.1$, (►) $a = 0.2$, (■) $a = 0.25$, (♦) $a = 0.5$, (★) $a = 1$, and (▲) $a = 2$; (- - -) $\tilde{T}^M/\tilde{T}_v = 6$.

$\tilde{t}/\tilde{T}_v \gtrsim 2$, the dynamics evolves toward the viscous regime defined by Eqs. (6) and (8) in a timescale depending on Re.

B. Scaling laws of the transient regime

As previously mentioned, the transient intermediate regime is reached and thus begins at $\tilde{t}/\tilde{T}_v \approx 2$. Unfortunately, its ending time is less obvious as it asymptotically evolves toward the purely viscous-dominated regime. Therefore, the intermediate regime can hardly be characterized, and we define the time $\tilde{T}^M/\tilde{T}_v \gtrsim 2$ at which the maximum deviation of the front position $\tilde{x}_f$ from the expected viscous solution $\tilde{x}_f^{\mathrm{th}|V}$ is obtained, i.e., $\tilde{x}_f^M = \max[(\tilde{x}_f - \tilde{x}_f^{\mathrm{th}|V})/\tilde{x}_f^{\mathrm{th}|V}]$ at $\tilde{t} = \tilde{T}^M$. Note that the timescales at which the minimum of $(\alpha - \alpha^{\mathrm{th}|V})/\alpha^{\mathrm{th}|V}$ and the maximum of $(\beta - \beta^{\mathrm{th}|V})/\beta^{\mathrm{th}|V}$ are reached can be slightly different from $\tilde{T}^M$ (more details given in Appendix). However, this does not reflect the general observations of the intermediate regime, and thus both α^M and β^M are estimated at $\tilde{T}^M$ here. Afterwards, the Reynolds number $\mathrm{Re} = a\mathrm{Re}^H$ is varied at constant $a = 0.5$ (red) and constant $\mathrm{Re}^H \sim 117$ (blue) with increasing Re^H and a, respectively, for ensuring the unique Re dependency of the slumping evolution.

Figure 9 shows the time ratio $\tilde{T}^M/\tilde{T}_v$ as a function of the Reynolds number Re, for numerical (closed symbols) and experimental (opened symbols) results. Here only data with $\mathrm{Re} > 10$ are considered as they clearly highlight an intermediate transient dynamics between the inertial slumping regime and the viscous-dominated one, as it will be argued later. One observes that the timescale $\tilde{T}^M$ of the intermediate regime scales with the transition time $\tilde{T}_v$. More specifically, we obtain $\tilde{T}^M/\tilde{T}_v \approx 6$ (dashed line) on the wide range of Re considered. Recall that it was previously reported that the transient regime begins at $\tilde{t}/\tilde{T}_v \approx 2$ (Sec. IV A). This supports that the timescale $\tilde{T}_v$ obtained by considering a sudden inertial-to-viscous transition remains the relevant timescale of the slumping evolution during the intermediate regime, even though both the front position and the shape of the slumping deviate from the viscous theoretical solution.

Prior discussing $\tilde{x}_f^M$, α^M, and β^M, the absolute extension of the slumping at $\tilde{t} = \tilde{T}^M$, i.e., $\tilde{x}_f(\tilde{T}^M)$, is first considered. Figure 10 shows that the Reynolds number Re is the relevant dimensionless parameter to collapse data on a master curve for both numerical simulations and laboratory experiments. More specifically, for $\mathrm{Re} > 10$, one obtains

$$\tilde{x}_f(\tilde{t} = \tilde{T}^M) \propto \mathrm{Re}^{1/3}. \tag{11}$$
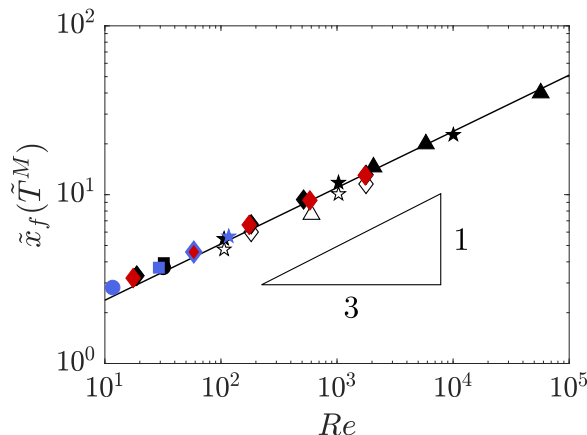
FIG. 10. Dimensionless front position $\tilde{x}_f(\tilde{T}^M)$ as a function of the Reynolds number Re, for numerical (closed symbols) and experimental (opened symbols) results. The red and blue colors correspond to the set of simulations at constant $a = 0.5$ and constant $\mathrm{Re}^H \sim 117$, respectively, while the symbols indicate the initial aspect ratio as (▼) $a = 0.05$, (●) $a = 0.1$, (▶) $a = 0.2$, (■) $a = 0.25$, (◆) $a = 0.5$, (★) $a = 1$, and (▲) $a = 2$.

In order to provide first clues on the obtained scaling, one recall that the intermediate regime is characterized by a timescale $\tilde{T}_v$ controlling both the initiation and the maximum deviation from the viscous regime. This suggests that the initiation of the intermediate regime is actually controlled by viscous dissipation. Moreover, the perturbative inertia remaining in the slumping pushes the slumping front and it then affects the inertial-to-viscous transition. A simple approach may be proposed to quantify the overshoot of the slumping front through a balance between horizontal inertia and viscous dissipation. As shown in Sec. III C, the inertia-dominated region evolves in space and time during the slumping. In order to simplify this observation for the purpose of scaling laws, we consider that inertia triggered by releasing the initial column should be completely dissipated by the work of viscous dissipation before reaching a unique balance between the pressure gradient and viscous friction, as stated by the viscous theoretical solution [Eqs. (6) and (8)]. This can be summarized as

$$\rho \frac{u_f^2}{x_f(T^M)} \sim \mu \frac{u_f}{h(x, T^M)^2}, \tag{12}$$

where $u_f \sim (gH)^{1/2}$ is the front velocity in the inertial slumping regime and $h(x, t)x_f(t) \sim HL$ is given by the mass conservation. Using the dimensionless form (Sec. III A), Eq. (12) can be rewritten as $\tilde{x}_f(\tilde{T}^M) \sim \mathrm{Re}^{1/3}$ in agreement with the scaling obtained above. Thus, it highlights that the intermediate regime is clearly controlled by a balance between inertia and viscous forces at the flow scale.

Along the same lines, Fig. 11 shows the influence of Re on the different extracted quantities $\tilde{x}_f^M$, α^M, and β^M, for numerical (closed symbols) and experimental (opened symbols) results. Again, this clearly shows that the Reynolds number Re is the relevant parameter to characterize the transient intermediate regime relatively to the viscous solution by collapsing data on master curves. More specifically, it is shown that $\tilde{x}_f^M$ and β^M (respectively, α^M) increase (respectively, decreases) with Re, for Re > 10, while no deviation of all quantities is obtained, otherwise. This confirms the previous estimate of a critical Reynolds number Re ≈ 10 for the appearance of an intermediate inertial-to-viscous regime. For Re > 10, the influence of the intermediate regime characterized through $\tilde{x}^M$, α^M and β^M is shown to increase with increasing Re. Finally, the combination of the obtained scaling $\tilde{x}_f(\tilde{T}^M) \sim \mathrm{Re}^{1/3}$ [Eq. (11)] and the viscous prediction [Eq. (6)] allows to predict the trend of $\tilde{x}_f^M$
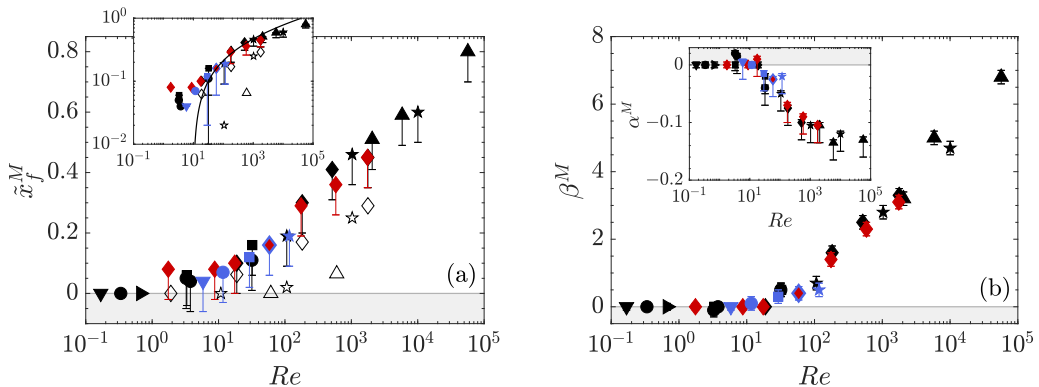
FIG. 11. Estimated quantities (a) $\tilde{x}_f^M$ (inset: log-log representation) and (b) β^M (inset: α^M) as a function of the Reynolds number Re for numerical (closed symbols) and experimental (opened symbols) results. The red and blue colors correspond to the set of simulations at constant $a = 0.5$ and constant $\mathrm{Re}^H \sim 117$, respectively, while the symbols indicate the initial aspect ratio as (▼) $a = 0.05$, (●) $a = 0.1$, (▶) $a = 0.2$, (■) $a = 0.25$, (◆) $a = 0.5$, (★) $a = 1$, and (▲) $a = 2$. In (a), the solid line indicates $\tilde{x}_f^M \sim \mathrm{Re}^{1/12} - 1$.

with Re. More specifically, one obtains $\tilde{x}_f^M \sim \mathrm{Re}^{1/12} - 1$ (solid line) in good agreement with data [inset of Fig. 11(a)].

V. LIMITATIONS AND OTHER REGIME

The flow dynamics of the slumping phase has been described in light of a single dimensionless parameter, namely the Reynolds number Re. These results are supported by the set of simulations at constant a (red) and constant Re^H (blue) with increasing Re^H and a, respectively, and thus increasing $\mathrm{Re} = a\mathrm{Re}^H$. Here the relevance of Re for describing the slumping dynamics is appropriate as the set of parameters covered mostly satisfies the two conditions mentioned in Sec. III A, i.e., $\mathrm{Re} > 1$ and $\mathrm{Re} > a^2$, as shown in Fig. 12. This suggests that the inertial-to-viscous transition occurs relatively far from the initial condition. Under the shallow-layer approximation, this allows to reduce the dynamics to a balance among hydrostatic pressure gradient, horizontal inertia, and viscous dissipation. Nevertheless, approaching the condition $\mathrm{Re} \sim a^2$ from below indicates that the validity of the shallow-layer approximation becomes questionable as the initial vertical inertia is non-neglibible on the flow dynamics. For $\mathrm{Re} < a^2$, it is even expected that inertia caused by the vertical falling of the fluid column becomes dominant during the transient dynamics, which leads probably to a balance between vertical fall and viscous dissipation. Hence, another dimensionless parameter should be defined to characterize the entire flow of the liquid phase. In particular, the aspect ratio a of the initial column may be interpreted as the vertical-to-horizontal inertia ratio.

In order to highlight such signature of a on the slumping dynamics, Fig. 13(a) shows the dimensionless front position $\tilde{x}_f$ as a function of the expected timescale $\tilde{t}$ according to the inertial solution [Eq. (5)], for $(\mathrm{Re}, a) = (\sim 10, 0.1)$ (solid line), $(\mathrm{Re}, a) = (\sim 20, 0.5)$ (dotted-dashed line) and $(\mathrm{Re}, a) = (\sim 10, 0.5)$ (dashed line), i.e., incrementally approaching the above-mentioned limit. Note that, in the case of a unique Re dependency, the global trend of $\tilde{x}_f$ should be equivalent here due to the limited range of Re considered, or at least the curves should be organized according to the values of Re. Such an observation is obtained at sufficiently long times where the front position $\tilde{x}_f$ propagates faster with increasing Re in consistence with the decrease of viscous dissipation. At early times, however, one clearly observes that the slumping dynamics cannot be fully described by considering solely the Reynolds number Re. In particular, the front position spreads faster with decreasing a (blue vs. red), regardless of Re. This observation may also be reported from the temporal evolution of the dimensionless height profile $\tilde{h}$, as shown in Fig. 13(b). This difference
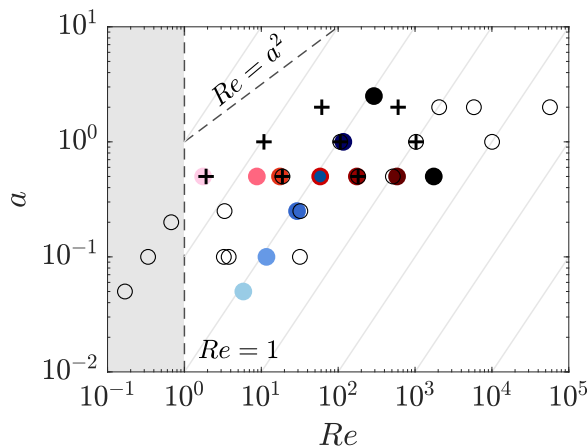
FIG. 12. Set of dimensionless parameters covered in the present study for both laboratory experiments (crosses) and numerical simulations (circles), in the (Re, a) plane. Full circles highlight the sets of simulations at constant $Re^H \sim 117$ (blue) and constant $a = 0.5$ (red) with increasing a and Re^H and thus increasing $Re = aRe^H$ (from light to dark colors), respectively. The light gray lines indicate the isovalue curves of Re^H from 1 (left) to 10^6 (right).

can be attributed to the relative influence of vertical inertia over horizontal inertia affecting the early stages of the collapsing dynamics of the fluid column.

Finally, it can be anticipated that the early stages of the slumping can prevail on the transient regime when a is increased, at constant Re. In this case, and more particularly for $a^2 > Re$, the obtained scalings for characterizing the transient intermediate regime are probably no longer valid. This would deserve further investigation, but it highlights that the couple (Re, a) should be considered to describe fully the slumping dynamics of a fluid column collapsing along an horizontal plane.
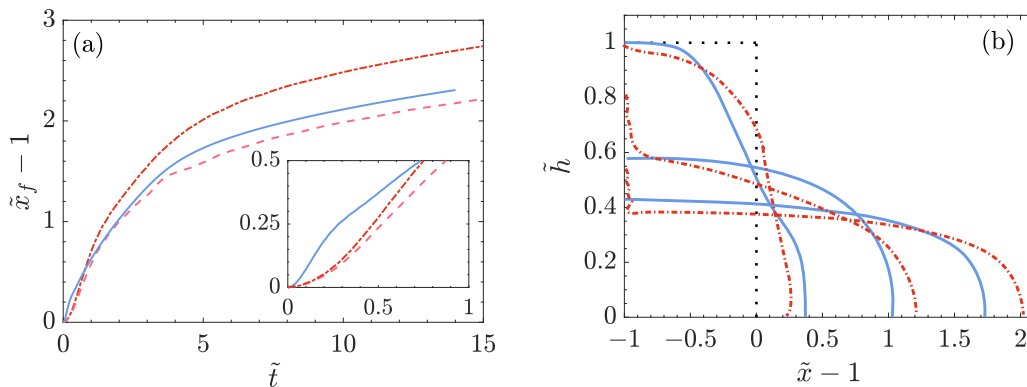
FIG. 13. (a) Temporal evolution of the dimensionless front position $\tilde{x}_f$ according to the inertial solution [Eq. (5)], for (Re, a) = ($\sim 10, 0.1$) (solid line), (Re, a) = ($\sim 20, 0.5$) (dotted-dashed line), and (Re, a) = ($\sim 10, 0.5$) (dashed line). (b) Dimensionless height profile $\tilde{h}$ as a function of the dimensionless streamwise direction $\tilde{x} - 1$, at $\tilde{t} = 0.5, 2$, and 5 for (Re, a) = ($\sim 10, 0.1$) (solid line) and (Re, a) = ($\sim 20, 0.5$) (dotted-dashed line).

VI. CONCLUSION

The propagation of horizontal dam-break flows from the initial inertial slumping toward the purely viscous regime has been investigated through numerical simulations and laboratory experiments, for which both the geometry of the initial column and the properties of the dense fluid released were systematically varied. In particular, an inertial-to-viscous transient dynamics has been highlighted and characterized as an intermediate regime in light of the Reynolds number Re. For Re $\lesssim$ 10, the transient dynamics vanishes: The front propagation and the shape of the current evolve progressively from an inertial solution toward a viscous one that can be prescribed by classical self-similar models obtained in the shallow layer limit. By contrast, for Re $\gtrsim$ 10, the front overshoots and then strongly decelerates accompanied by a deficit and an excess of fluid at the origin and at the front, respectively, relatively to the viscous asymptotic solution obtained at longer times. Surprisingly, an inertial-to-viscous transition timescale estimated by balancing the inertial and viscous self-similar solutions remains the relevant timescale controlling both the initiation and the maximum deviation of the intermediate regime relatively to the viscous one. One has shown that the transient intermediate regime is mostly controlled by the Reynolds number Re in the range of parameters considered. In particular, the absolute extension of the slumping, at which the maximum overshoot characterizing the transient regime is obtained, scales as $\mathrm{Re}^{1/3}$ interpreted as the length over which the initial inertia is fully dissipated by the work of viscous dissipation. Likewise, the maximum overshoot of the front position and the associated relative front shape have been shown to scale with Re. All together, these results suggest that a transient regime has to be considered for improving the modeling of unsteady gravity-driven flows in industrial and geophysical applications.

APPENDIX: ESTIMATE OF THE TIMESCALE $\tilde{T}^M$

In the present study, the timescale of the transient intermediate regime is estimated as the time $\tilde{T}^M$ at which the maximum deviation of the front position $\tilde{x}_f$ from the expected viscous solution $\tilde{x}_f^{\mathrm{th}|V}$ is
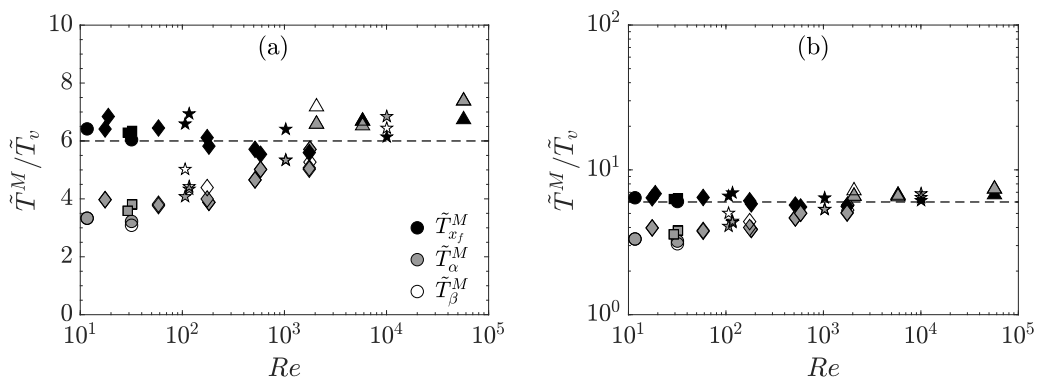
FIG. 14. Timescale ratio $\tilde{T}^M/\tilde{T}_v$ as a function of the Reynolds number Re with (a) log-lin and (b) log-log representations, where $\tilde{T}^M$ is defined as the timescales at which the maximum value of $(\tilde{x}_f - \tilde{x}_f^{\mathrm{th}|V})/\tilde{x}_f^{\mathrm{th}|V}$ (black symbols) and $(\beta - \beta^{\mathrm{th}|V})/\beta^{\mathrm{th}|V}$ (white symbols), and the minimum values of $(\alpha - \alpha^{\mathrm{th}|V})/\alpha^{\mathrm{th}|V}$ (gray symbols) are obtained when $\tilde{t}/\tilde{T}_v \gtrsim 2$, noted as $\tilde{T}_{xf}^M$, $\tilde{T}_\beta^M$, and $\tilde{T}_\alpha^M$, respectively. The symbols indicate the initial aspect ratio as (●) $a = 0.1$, (▶) $a = 0.2$, (■) $a = 0.25$, (◆) $a = 0.5$, (★) $a = 1$, and (▲) $a = 2$; (- - -) $\tilde{T}^M/\tilde{T}_v = 6$.
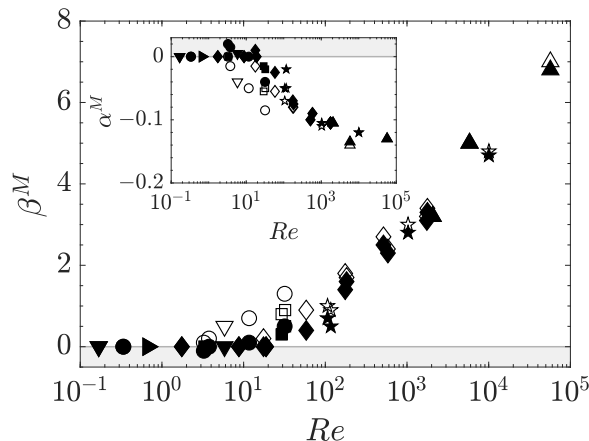
FIG. 15. β^M (inset: α^M) estimated as the value of $(\beta - \beta^{\text{th}|V})/\beta^{\text{th}|V}$ (inset: $(\alpha - \alpha^{\text{th}|V})/\alpha^{\text{th}|V}$) at $\tilde{t} = \tilde{T}^M_{x_f}$ (closed symbols) and $\tilde{t} = \tilde{T}^M_\beta$ (inset: $\tilde{t} = \tilde{T}^M_\alpha$) (opened symbols). The symbols indicate the initial aspect ratio as (●) $a = 0.1$, (▶) $a = 0.2$, (■) $a = 0.25$, (◆) $a = 0.5$, (★) $a = 1$, and (▲) $a = 2$.

obtained. Accordingly, both quantities α^M and β^M are defined as the deviation of $(\alpha - \alpha^{\text{th}|V})/\alpha^{\text{th}|V}$ and $(\beta - \beta^{\text{th}|V})/\beta^{\text{th}|V}$ at $\tilde{t} = \tilde{T}^M$, respectively. Nevertheless, the time $\tilde{T}^M$ could also be estimated from the minimum and maximum of the other quantities $(\alpha - \alpha^{\text{th}|V})/\alpha^{\text{th}|V}$ and $(\beta - \beta^{\text{th}|V})/\beta^{\text{th}|V}$, respectively. Figure 14 shows the timescale ratio $\tilde{T}^M/\tilde{T}_v$ as a function of Re with (a) log-lin and (b) log-log representations, where $\tilde{T}^M$ is estimated as the time at which the maximum values of $(\tilde{x}_f - \tilde{x}_f^{\text{th}|V})/\tilde{x}_f^{\text{th}|V}$ (black symbols) and $(\beta - \beta^{\text{th}|V})/\beta^{\text{th}|V}$ (white symbols), and the minimum value of $(\alpha - \alpha^{\text{th}|V})/\alpha^{\text{th}|V}$ (gray symbols) are obtained when $\tilde{t}/\tilde{T}_v \gtrsim 2$, noted as $\tilde{T}^M_{x_f}$, $\tilde{T}^M_\beta$, and $\tilde{T}^M_\alpha$, respectively. Overall, the order of magnitude of $\tilde{T}^M/\tilde{T}_v$ is similar with the different extracted methods. Additionally, the values of $\tilde{T}^M_\alpha$ and $\tilde{T}^M_\beta$ are close each other because both are extracted from the shape of the height profile of the slumping. By contrast, some quantitative differences can be reported between $\tilde{T}^M_{x_f}$ and both $\tilde{T}^M_\alpha$ and $\tilde{T}^M_\beta$, for Re $\lesssim 10^3$, which are not observed, for Re $\gtrsim 10^3$.

The influence of the extracted method of $\tilde{T}^M$ on the scaling laws of the different quantities can be then addressed by considering β^M (respectively, α^M) estimated as the value of $(\beta - \beta^{\text{th}|V})/\beta^{\text{th}|V}$ [respectively, $(\alpha - \alpha^{\text{th}|V})/\alpha^{\text{th}|V}$] at $\tilde{t} = \tilde{T}^M_{x_f}$ and $\tilde{t} = \tilde{T}^M_\beta$ (respectively, $\tilde{t} = \tilde{T}^M_\alpha$), as shown by closed and opened symbols, respectively, in Fig. 15. Recall that T^M_α and T^M_β are roughly equal on the range of Re considered (Fig. 14). Overall, a similar trend of β^M (respectively, α^M) is obtained with the two methods, and the conclusions of the paper are therefore unchanged. Additionally, a more important scatter of data is obtained by estimating α^M and β^M at $\tilde{t} = \tilde{T}^M_\alpha$ and $\tilde{t} = \tilde{T}^M_\beta$, respectively, compared to their estimate at $\tilde{t} = \tilde{T}^M_{x_f}$ as considered in the paper. The measures are thus aimed at improving the results quantitatively without affecting the analyses and the conclusions.

[1] R. Delannay, A. Valance, A. Mangeney, O. Roche, and P. Richard, Granular and particle-laden flows: From laboratory experiments to field observations, J. Phys. D **50**, 053001 (2017).

[2] N. Roussel and P. Coussot, "fifty-cent rheometer" for yield stress measurements: From slump to spreading flow, J. Rheol. **49**, 705 (2005).

[3] N. J. Balmforth, R. V. Craster, P. Perona, A. C. Rust, and R. Sassi, Viscoplastic dam breaks and the Bostwick consistometer, J. Non-Newton. Fluid Mech. **142**, 63 (2007).

[4] A. Ritter, Die fortpflanzung der wasserwellen, Z. Verein Deutch. Ing. **36**, 947 (1892).

[5] H. E. Huppert, The propagation of two-dimensional and axisymmetric viscous gravity currents over a rigid horizontal surface, J. Fluid Mech. **121**, 43 (1982).

[6] P. K. Stansby, A. Chegini, and T. C. D. Barnes, The initial stages of dam-break flow, J. Fluid Mech. **374**, 407 (1998).

[7] J. W. Rottman and J. E. Simpson, Gravity currents produced by instantaneous releases of a heavy fluid in a rectangular channel, J. Fluid Mech. **135**, 95 (1983).

[8] E. Lajeunesse, J. B. Monnier, and G. M. Homsy, Granular slumping on a horizontal surface, Phys. Fluids **17**, 103302 (2005).

[9] G. Lube, H. E. Huppert, R. S. J. Sparks, and A. Freundt, Collapses of two-dimensional granular columns, Phys. Rev. E **72**, 041301 (2005).

[10] J. M. Piau and K. Debiane, Consistometers rheometry of power-law viscous fluids, J. Non-Newton. Fluid Mech. **127**, 213 (2005).

[11] C. Ancey, N. Andreini, and G. Epely-Chauvin, The dam-break problem for concentrated suspensions of neutrally buoyant particles, J. Fluid Mech. **724**, 95 (2013).

[12] D. Dumont, M. Houze, P. Rambach, T. Salez, S. Patinet, and P. Damman, Emergent Strain Stiffening in Interlocked Granular Chains, Phys. Rev. Lett. **120**, 088001 (2018).

[13] A. Bougouin, L. Lacaze, and T. Bonometti, Collapse of a liquid-saturated granular column on a horizontal plane, Phys. Rev. Fluids **4**, 124306 (2019).

[14] A. Abramian, L. Staron, and P.-Y. Lagrée, The slumping of a cohesive granular column: Continuum and discrete modeling, J. Rheol. **64**, 1227 (2020).

[15] L. Brezzi, F. Gabrieli, and S. Cola, Collapse of granular–cohesive soil mixtures on a horizontal plane, Acta Geotech. **15**, 695 (2020).

[16] L. Lacaze, J. Bouteloup, B. Fry, and E. Izard, Immersed granular collapse: From viscous to free-fall unsteady granular flows, J. Fluid Mech. **912**, A15 (2021).

[17] G. Lauber and W. H. Hager, Experiments to dambreak wave: Horizontal channel, J. Hydraul. Res. **36**, 291 (1998).

[18] I. M. Jánosi, D. Jan, K. G. Szabó, and T. Tél, Turbulent drag reduction in dam-break flows, Exp. Fluids **37**, 219 (2004).

[19] J. G. Leal, R. M. Ferreira, and A. H. Cardoso, Dam-break wave-front velocity, J. Hydraul. Eng. **132**, 69 (2006).

[20] O. Roche, S. Montserrat, Y. Niño, and A. Tamburrino, Experimental observations of water-like behavior of initially fluidized, dam break granular flows and their relevance for the propagation of ash-rich pyroclastic flows, J. Geophys. Res. **113**, B12 (2008).

[21] T. Bonometti, S. Balachandar, and J. Magnaudet, Wall effects in non-Boussinesq density currents, J. Fluid Mech. **616**, 445 (2008).

[22] A. Bougouin, L. Lacaze, and T. Bonometti, Collapse of a neutrally buoyant suspension column: From Newtonian to apparent non-Newtonian flow regimes, J. Fluid Mech. **826**, 918 (2017).

[23] R. F. Dressler, Hydraulic resistance effect upon the dam-break functions, J. Res. Natl. Bur. Stan. **49**, 217 (1952).

[24] R. F. Dressler, Comparison of theories and experiments for the hydraulic dam-break wave, Int. Assoc. Sci. Hydrol. **3**, 319 (1954).

[25] A. J. Hogg and A. W. Woods, The transition from inertia- to bottom-drag-dominated motion of turbulent gravity currents, J. Fluid Mech. **449**, 201 (2001).

[26] A. J. Hogg and D. Pritchard, The effects of hydraulic resistance on dam-break and other shallow inertial flows, J. Fluid Mech. **501**, 179 (2004).

[27] T. V. Ball and H. E. Huppert, Similarity solutions and viscous gravity current adjustment times, J. Fluid Mech. **874**, 285 (2019).

[28] J. J. Webber and H. E. Huppert, Time to approach similarity, Q. J. Mech. Appl. Math. **73**, 1 (2020).

[29] L. A. Amy, A. J. Hogg, J. Peakall, and P. J. Talling, Abrupt transitions in gravity currents, J. Geophys. Res. Earth Surf. **110**, F03001 (2005).

[30] A. J. Hogg, Lock-release gravity currents and dam-break flows, J. Fluid Mech. **569**, 61 (2006).

[31] H. G. Weller, G. Tabor, H. Jasak, and C. Fureby, A tensorial approach to computational continuum mechanics using object-oriented techniques, Comput. Phys. **12**, 620 (1998).

[32] A. Bougouin, Etude expérimentale de l'effondrement d'une colonne fluide-grains, Institut National Polytechnique de Toulouse, Ph.D. thesis, 2017.

[33] Y. Liu, N. J. Balmforth, S. Hormozi, and D. R. Hewitt, Two–dimensional viscoplastic dambreaks, J. Non-Newton. Fluid Mech. **238**, 65 (2016).

[34] W. Sarlin, C. Morize, A. Sauret, and P. Gondret, Collapse dynamics of dry granular columns: From free-fall to quasistatic flow, Phys. Rev. E **104**, 064904 (2021).